



Dual-interface engineering induced by silane coupling agents with different functional groups constructing high-performance flexible perovskite solar cells



Zijun Yi, Xin Li*, Bo Xiao, Qinghui Jiang, Yubo Luo, Junyou Yang*

State Key Laboratory of Material Processing and Die & Mould Technology, Huazhong University of Science and Technology, Wuhan 430074, PR China

ARTICLE INFO

Keywords:
Flexible perovskite solar cells
Tin dioxide
Silane coupling agents
Dual-interface passivation

ABSTRACT

Defect-induced charge non-radiative recombination loss at perovskite/charge transport layers (CTLs) interfaces greatly deteriorates the efficiency and stability of flexible perovskite solar cells (PSCs). Therefore, a comprehensive strategy for reducing the defect density both at perovskite/CTLs interfaces is urgently required. Herein, the 1-[3-(Trimethoxysilyl)propyl]urea (TMPU) material is adopted to improve the conductivity of SnO₂ and passivate the unfavorable SnO₂/perovskite interface defects. Meanwhile, the trimethoxy(3,3,3-trifluoropropyl) silane (TMFS) layer is employed at perovskite/spiro-OMeTAD interface for the sake of suppressing the surface defects of perovskite and ameliorating environmental stability of the perovskite. Such a dual-interface engineering strategy is beneficial to significantly reduce interface defect density and unfavorable non-radiative recombination loss, thus achieving faster transport and effective collection of carriers. Consequently, the optimized flexible and rigid PSCs yield outstanding photoelectric conversion efficiency (PCE) of 20.06% and 23.11%, respectively, which are both significantly higher than the pristine devices. Notably, the target flexible device presents excellent mechanical durability and retains 91.3% of the initial PCE after 5000 bending cycles with bending radius of 10 mm.

1. Introduction

For the past few years, flexible perovskite solar cells (PSCs) have aroused widespread attention from its potential power supply to wearable electronic devices [1–6]. Encouragingly, the highest photoelectric conversion efficiency (PCE) of current rigid PSCs has reached 25.8%, which is comparable to the photovoltaic (PV) performance of commercial silicon solar cells [7,8]. However, the PCE and operational stability of flexible PSCs are still far inferior to the rigid counterparts prepared on glass substrates. Thus, there is no doubt that effective and reasonable measures need to be implemented to further improve the PV performance of flexible PSCs.

Generally speaking, the charge transport layers (CTLs) are indispensable functional layers in typical PSC structures, which acts as the extraction and transport of photogenerated carriers in both rigid and flexible device [9–11]. Previous studies have demonstrated that the existence of defects at perovskite/CTLs interfaces will lead to severe non-radiative recombination by trapping electron and hole carriers, which consequently brings about energy losses and impairs the PCE of

PSCs [12,13]. On the one hand, the SnO₂ has been currently considered as an ideal electron transport layer (ETL) candidate in flexible PSCs owing to its low temperature preparation advantages [14]. It is worth noting that flexible plastic substrates exhibit higher surface roughness and film resistance compared to rigid substrates [15]. Unfortunately, the SnO₂ films deposited on the surface of flexible substrates under low temperature conditions will inevitably induce some unfavorable intrinsic defects (such as uncoordinated Sn²⁺ and oxygen vacancy defects), which can greatly deteriorate the electrical properties and surface quality of SnO₂ [16]. Even worse, the unfavorable SnO₂ film quality has a detrimental effect on the growth of the upper perovskite, resulting in the generation of numerous perovskite/SnO₂ interface defects and severe interfacial non-radiative recombination loss [17–19]. On the other hand, the 2,2',7,7'-tetrakis(N,N-di-p-methoxyphenylamine)-9,9'-spirobifluorene (spiro-OMeTAD) compound is widely employed as hole transport layer (HTL) for high-performance PSCs [20]. In particular, the mixed cations perovskite due to ionic properties will lead to evaporation of organic components from the surface and the spiro-OMeTAD HTL suffers from inferior electrical properties, thus causing worse

* Corresponding authors.

E-mail addresses: xin_li@hust.edu.cn (X. Li), jyyang@mail.hust.edu.cn (J. Yang).

perovskite/spiro-OMeTAD interfacial contact and higher energy barrier between perovskite with spiro-OMeTAD [21,22]. Based on the above facts, the dual-interface engineering is definitely a more feasible strategy to simultaneously reduce the defects at both perovskite/CTLs interfaces and achieve efficient carrier extraction. For instance, Song et al. reported that the Nb_2CT_x ($x = \text{OH}, \text{O}$) nanosheets were employed to reduce interface energy-levels offsets [23]. Chen et al. also demonstrated that the (3-aminopropyl) trimethoxy silane (APTMS) was beneficial to minimize both SnO_2 /perovskite and perovskite/spiro-OMeTAD interfaces defects [24]. By now, the above-mentioned strategy is only implemented on rigid device, rarely reported in flexible PSCs. Thus, it is urgent to develop comprehensive strategies to modulate perovskite/CTLs interfaces in flexible PSCs. Silane coupling agents have a common formula of $\text{Y}-\text{R}-\text{Si}-\text{X}_3$, where Y is an organic functional group, R is an alkylidene group and X is a hydrolyzable group, which can be used as interfacial connection materials for inorganic and organic semiconductors due to the special properties of the groups [25,26]. The two key interfaces of flexible PSCs are positively affected by adjusting the organic functional groups of the silane coupling agents. Additionally, silane coupling agents generally have unique heat dissipation effects, which are beneficial to achieve great thermal management of flexible PSCs. Therefore, the application of silane coupling agents on flexible PSCs to address interface issues is highly desirable.

Herein, we devise a dual-interface engineering strategy induced by silane coupling agents to ameliorate perovskite/CTLs interfaces and reduce non-radiative carrier recombination loss in flexible PSCs. The 1-[3-(Trimethoxysilyl)propyl]urea (TMPU) is used as an interfacial material at SnO_2 /perovskite interface. It is uncovered that the adoption of TMPU interface layer is beneficial to suppress the surface defects of SnO_2 by forming Sn-O-Si bonds, thus improving the conductivity of SnO_2 film and obtaining better perovskite film quality. Together, the trimethoxy (3,3,3-trifluoropropyl)silane (TMFS) material with trifluoromethyl group ($-\text{CF}_3$) is employed to regulate perovskite/spiro-OMeTAD interface, which is conducive to passivating detrimental interface defects and facilitating faster carrier extraction. The flexible PSCs based on the above dual-interface engineering effects yield a higher open-circuit voltage (V_{OC}) of 1.16 V and PCE of 20.06% than the pristine device with a PCE of 16.44%. Remarkably, the optimal flexible PSCs can retain 86.1% of the initial PCE after storing at $50 \pm 5\%$ relative humidity (RH) for 3000 h and display outstanding mechanical endurance with 91.3% of the original efficiency retention after 5000 bending cycles. In addition, the rigid PSCs modified by silane coupling agents interface layers produce an excellent PCE of 23.11%.

2. Experimental

2.1. Materials

Polyethylene naphthalate/tin-doped indium oxide (PEN/ITO) flexible substrates, spiro-OMeTAD powder, N, N-dimethylformamide (DMF), isopropanol (IPA), dimethyl sulfoxide (DMSO), and chlorobenzene were obtained from Youxuan company. Lead iodide (PbI_2), formamidinium iodide (FAI), cesium iodide (CsI), lead bromide (PbBr_2), methylammonium bromide (MABr), 4-*tert*-butylpyridine (TBP) solution and bis(trifluoromethane) sulfonimide lithium salt (Li-TFSI) material were bought from Xi'an Polymer Light Technology Corp. The SnO_2 colloidal dispersion (15% in H_2O) was purchased from Alfa Aesar. The 1-[3-(Trimethoxysilyl)propyl]urea (TMPU) and trimethoxy(3,3,3-trifluoropropyl)silane (TMFS) powders were obtained from Aladdin.

2.2. Device fabrication

The flexible substrates were immersed in an ethanol solution for ultrasonic cleaning for 15 min before use. Then, the 1 mL of commercial SnO_2 colloidal dispersion was mixed with 5 mL of deionized water to obtain the SnO_2 solution. After that, 80 μL of SnO_2 solution was spin

coated onto the PEN/ITO flexible substrate at 3000 rpm for 30 s and then annealed at 150 °C for 30 min. The flexible substrates were immersed in different concentration solutions of TMPU in IPA for 3 h to obtain a TMPU layer, and heated at 100 °C for 10 min. The perovskite solution with the chemical formula $\text{Cs}_{0.05}(\text{FA}_{0.95}\text{MA}_{0.05})_{0.95}\text{Pb}(\text{I}_{0.95}\text{Br}_{0.05})_3$ was prepared by mixing PbI_2 (572 mg), FAI (196 mg), MABr (13 mg), PbBr_2 (22 mg), CsI (16 mg) of these powders in 1 mL of solvent (DMF: DMSO = 4:1), and stirred for several hours before use. Then, the 50 μL of above perovskite solution was deposited onto the surface of TMPU film by spin coating at 4000 rpm for 30 s, while the chlorobenzene (180 μL) as an anti-solvent was simultaneously dripped quickly at 15th second in this stage, and treated at 100 °C for 60 min. After cooled down, the different concentration solutions of TMFS in IPA were spin coated on the surface of perovskite film at 3000 rpm for 30 s. Subsequently, the substrates were transferred on a heater and treated at 100 °C for additional 10 min. Afterward, the preparation procedures for spiro-OMeTAD HTL and Au electrode were consistent with our previous reports [27,28]. Additionally, the fabrication process for rigid PSCs was similar to the flexible devices described above.

2.3. Characterization

The X-ray diffraction (XRD) patterns of perovskite films were collected by a diffractometer (X'Pert PRO, PANalytical). X-ray photoelectron spectroscopy (XPS) and Ultraviolet photoelectron spectroscopy (UPS) characterizations were performed using XPS/UPS system (AXIS-ULTRA DLD-600 W, Shimadzu). The scanning electron microscope (SEM, model of Nova Nano SEM 450) was employed to observe the morphology of the films. The surface roughness and potentials of films were obtained with the instrument of atomic force microscope (AFM, SPM9700). The ultraviolet-visible (UV) spectrophotometer (model of Lambda 950, Perkin Elmer) was employed to record the absorption spectra of different films. The LabRAM HR800 and fluorescence spectrometer (model of FLS980, Edinburgh) were used to observe the steady-state photoluminescence (PL) and time-resolved photoluminescence (TRPL) spectra of films. The current density–voltage (J-V) curves of the flexible and rigid PSCs were characterized by a Keithley 2400 source meter under AM 1.5G irradiation (light intensity of 100 mW cm^{-2}). The effective test area of the device is 0.06 cm^2 . The Newport-74125 system was employed to collect the incident photon-electron conversion efficiency (IPCE) spectra.

3. Results and discussion

As shown in Fig. 1a, the molecular structure of TMPU compound contains siloxane chain, amino group ($-\text{NH}_2$) and carbonyl group ($-\text{C=O}$). The TMPU layer is prepared by immersing the SnO_2 substrate in a solution of TMPU in IPA to induce spontaneous adsorption of TMPU molecules onto the surface of SnO_2 , as depicted in Fig. 1b. To confirm whether the TMPU molecule is effectively deposited on the surface of SnO_2 , XPS spectroscopy measurements are performed in Fig. 1c and d. Evidently, the XPS peak positions at 102.58 eV and 399.95 eV are attributed to Si and N elements, thus verifying the effective presence of TMPU molecule on the surface of SnO_2 [29]. Meanwhile, the XPS is further performed to investigate the interaction of TMPU and SnO_2 through the binding energy changes of the elements (Table S1). As presented in Fig. 1e and f, the Sn 3d and O 1s XPS peaks are shifted toward higher binding energies compared to the pristine, suggesting a possible interaction between TMPU and SnO_2 . The peak fitting is implemented to further explore the interaction of TMPU and SnO_2 . Obviously, the surface of SnO_2 treated with TMPU material will affect the Sn chemical environment, which is mainly reflected in the reduction of the Sn^{2+} ratio and the corresponding suppression of unfavorable Sn dangling bonds defects in the initial SnO_2 film. As previously reported, another detrimental crystal defect (oxygen vacancy defect) is also present in SnO_2 film, which greatly limits electron transfer in SnO_2 ETL

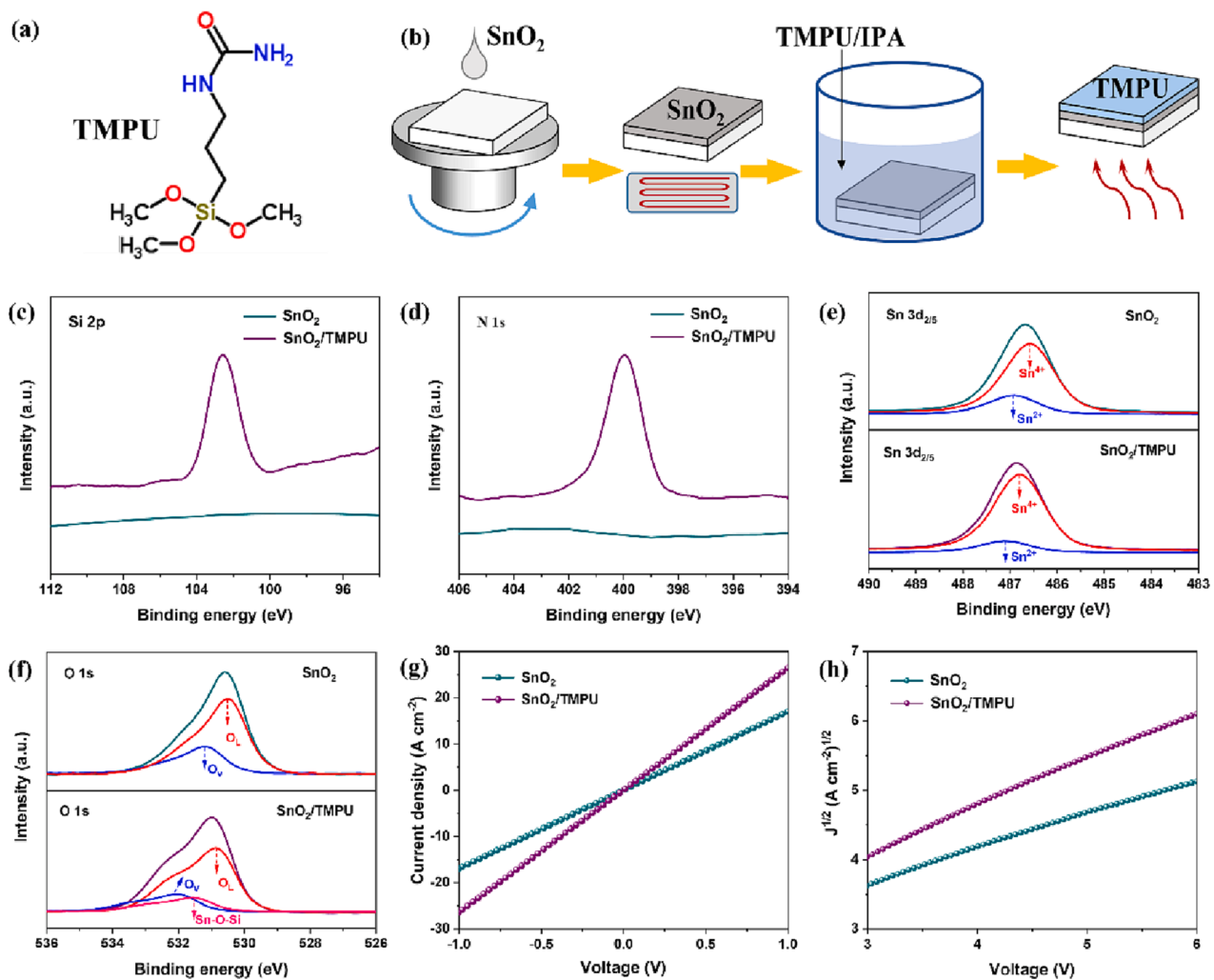


Fig. 1. (a) The molecular structure of TMPU. (b) The preparation procedure of TMPU layer. (c) Si 2p, (d) N 1s, (e) Sn 3d and (f) O 1 s XPS spectra of SnO₂ and SnO₂/TMPU films. (g) The conductivity and (h) electron mobility measurements of SnO₂ and SnO₂/TMPU films.

[16]. The oxygen vacancy (O_V) ratio of SnO₂ film after TMPU modification is reduced from 26.28% to 15.31%, which is a favorable signal for decreasing surface defects in SnO₂ (Table S2). The principle that the presence of TMPU facilitates the suppression of crystal defects in SnO₂ may be due to the condensation reaction between the hydrolyzed siloxane group in the TMPU molecule and hydroxyl groups on the SnO₂ surface to form the Sn-O-Si bond, whose XPS peak position is located at 531.53 eV in Fig. 1f [30–32]. The surface roughness of the SnO₂ and SnO₂/TMPU films are explored by AFM instrument (Fig. S1). The root mean square (RMS) roughness of pristine SnO₂ film is decreased from 7.52 nm to 6.28 after TMPU modification. Additionally, the thickness of the TMPU layer was determined by a step meter to be approximately 2.13 nm after removing the influence of the substrate. The conductivity of ETL is calculated using the formula of $\sigma = Id/VA$, where A and d represent the effective test area and thickness of the ETL, respectively. Apparently, the conductivity of SnO₂ film is increased from an initial 5.14×10^{-5} S·cm⁻¹ to 8.42×10^{-5} S·cm⁻¹ after TMPU modification (Fig. 1g) [33]. Furthermore, the electron mobility of ETLs are determined according to the equation: $J = 9\epsilon_0\epsilon_s\mu V^2/(8d^3)$, where μ represents the electron mobility of ETLs, ϵ_0 and ϵ_s specify the dielectric constant and vacuum dielectric constant of ETLs, respectively (Fig. 1h) [27]. The electron mobility of the SnO₂/TMPU films is estimated to be 6.95×10^{-4} cm²·V⁻¹·s⁻¹ compared to the bare SnO₂ (3.79×10^{-4} cm²·V⁻¹·s⁻¹). It is clear that the electrical properties of SnO₂ are improved after TMPU modification originated from the reduction of the

corresponding surface defects and the probability of carrier trapping. In the following, the influence of TMPU on the conduction band (E_C) and valence band (E_V) positions of SnO₂ is probed by UPS measurements, where the calculation of E_C and E_V positions can be consulted in previous literature [34]. The E_C and E_V can be estimated to be -4.23 eV and -8.01 eV for the SnO₂/TMPU, respectively, while E_C and E_V of the initial SnO₂ are determined to be -4.35 eV and -8.13 eV, respectively (Fig. S2). In particular, the results of UPS measurements are further verified using the Kelvin probe force microscope (KPFM) (Fig. S3). Noticeably, a higher surface potential is observed in SnO₂/TMPU film than the pure SnO₂ film, thus confirming the higher Fermi level (E_f) for SnO₂/TMPU film [27]. In short, the SnO₂ modified with TMPU is conducive to improving electrical properties and establishing suitable energy level match with perovskite, thereby contribute to reducing energy loss and achieving more favorable electron transfer in flexible PSCs.

For regular (n-i-p) flexible PSCs, the surface morphology of perovskite film is closely associated with the SnO₂ ETL at the bottom [35]. Thus, the AFM and SEM images are further collected to explore the influences of TMPU interlayer on perovskite films (Fig. S4 and S5). Clearly, a lower surface roughness (23.52 nm) is observed in perovskite film in the presence of TMPU than the pristine (27.68 nm). Especially, the perovskite film deposited on the SnO₂/TMPU presents a larger average grain size (472 nm) than the pristine perovskite film (317 nm). As displayed in Fig. 2a, the perovskite film based on SnO₂/TMPU presents enhanced UV-visible light absorption, mainly attributing to the

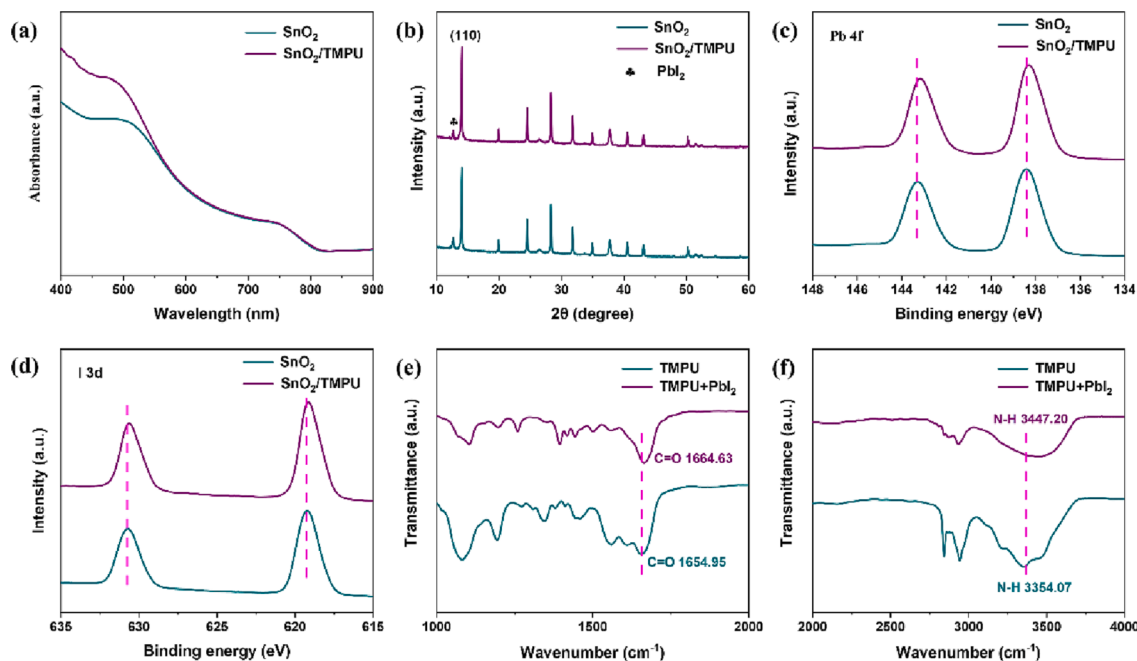


Fig. 2. (a) The absorption curves and (b) XRD patterns of the perovskite films based on SnO_2 and SnO_2/TMPU . The XPS peaks of (c) Pb 4f, and (d) I 3d for perovskite films based on SnO_2 and SnO_2/TMPU . The FTIR spectra between TMPU and PbI_2 in the wavenumber of (e) 1000 cm^{-1} — 2000 cm^{-1} , (f) 2000 cm^{-1} — 4000 cm^{-1} .

reduced surface roughness and improved perovskite film quality. Based on the above phenomena, we speculate that the corresponding microscopic mechanisms can be interpreted from the perspective of molecular interactions. The XRD patterns of perovskite films based on bare and TMPU-modified SnO_2 layer are depicted in Fig. 2b. Apparently, the perovskite film based on SnO_2/TMPU exhibits better crystallinity compared to the initial. It is noteworthy that the diffraction peak of PbI_2 at 12.6° slightly decreases in the case of TMPU modification. As reported, the slight excess of PbI_2 is conducive to passivating the detrimental defects of perovskite film, however, excessive PbI_2 also impair the stability of perovskite [16]. Therefore, it is conjectured that the TMPU molecule can modulate the formation of PbI_2 to optimize the microscopic morphology of perovskite film. To verify this hypothesis, the XPS characterizations are measured to probe the potential interactions between TMPU and PbI_2 . As revealed in Fig. 2c and d, the Pb 4f and I 3d XPS peaks of perovskite film deposited on SnO_2/TMPU are shifted to lower binding energies, showing a possible interaction between TMPU and perovskite. Through analysis, the amino ($-\text{NH}_2$) and carbonyl ($-\text{C=O}$) functional groups of the TMPU molecule can donor electrons to the uncoordinated Pb^{2+} based on Lewis acid-base interactions, thus affecting the local chemical environment of Pb and I [36]. Additionally, the FTIR spectroscopy is carried out to further uncover the positive effects between the two functional groups in TMPU and PbI_2 . As presented in Fig. 2e and f, the C=O stretching vibration peak is shifted to 1664.63 cm^{-1} compared to pure TMPU (1654.95 cm^{-1}) when the TMPU is mixed with PbI_2 . The N-H peak in TMPU is also changed to 3447.20 cm^{-1} after blending with PbI_2 . In brief, the synergistic NH_2 and C=O groups of TMPU is beneficial to interact with PbI_2 by Lewis acid-base interaction, thus reducing the proportion of under-coordinated Pb^{2+} cations and passivating the unfavorable antisite Pb defects [37]. Meanwhile, the functional group effect of TMPU also provides favorable conditions for the crystallization of perovskite film, thereby obtaining the perovskite film with better crystallinity [38]. The trap-filling limit voltage (V_{TFL}) is related with the trap-state density (N_t) of the device using the functional formula: $N_t = 2\varepsilon_r\varepsilon_0 V_{\text{TFL}} / (qL^2)$, where q and L are the charge unit and thickness of perovskite films, respectively [39]. The device with SnO_2/TMPU presents a lower trap density of $3.62 \times 10^{15}\text{ cm}^{-3}$ than the pristine device based on SnO_2 (5.23×10^{15}

cm^{-3}), thus confirming that the TMPU interface layer is conducive to inhibiting the overall defects in SnO_2 and perovskite films (Fig. S6).

Combined with UPS results, the SnO_2 treated with TMPU exhibits better energy level matching for efficient electron transfer (Fig. 3a). The above conclusions can be further supported by PL and TRPL spectra measurements, as displayed in Fig. 3b and Fig. S7. The reduced PL intensity of perovskite film based on SnO_2/TMPU is observed, reflecting that the introduction of TMPU layer could notably enhance electron extraction and transfer [27]. The TRPL datas are further fitted according to the equation of $I(t) = A_1 \exp(-t/\tau_1) + A_2 \exp(-t/\tau_2)$, where τ_1 stands for the fast decay time constant for interface charge transfer and τ_2 represents the slow decay time constant in perovskite films [40]. The perovskite film based on SnO_2/TMPU presents a shorter lifetime ($\tau_1 = 17.63\text{ ns}$, $\tau_2 = 92.86\text{ ns}$) than the pristine perovskite film ($\tau_1 = 25.38\text{ ns}$, $\tau_2 = 142.27\text{ ns}$), proofing more effective electron transfer in perovskite film after TMPU modification. The effect of different concentrations of TMPU on PV performance of flexible PSCs is evaluated by device preparation, as revealed in Fig. 3c and Table S3. For the pristine device with the bare SnO_2 , the obtained PCE is 16.44% with a V_{OC} of 1.06 V , a short-circuit current density (J_{SC}) of 22.13 mA cm^{-2} and a fill factor (FF) of 70.08%. In contrast, the champion flexible PSCs with optimized concentration (5 mM) of TMPU achieves a higher PCE of 18.41%, accompanied with an V_{OC} of 1.12 V , a J_{SC} of 22.32 mA cm^{-2} and a FF of 73.65%. The integrated current value of flexible device based on SnO_2/TMPU is 22.26 mA cm^{-2} determined from the IPCE spectra, which is line with the J_{SC} measured from the J-V curve (Fig. 3d). The PCE of the champion flexible device using SnO_2/TMPU stabilizes at 18.35%, which is basically consistent with the measurement of the J-V sweep (Fig. 3e). As observed in Fig. 3f, the repeatability of flexible devices with SnO_2/TMPU is confirmed by PCE statistics of about 25 solar cells.

To further enhance the PV performance of the above flexible PSCs, the modulation of perovskite/spiro-OMeTAD interface, which plays a dominant role in hole extraction and separation, is equally critical compared to the $\text{SnO}_2/\text{perovskite}$ interface [23]. Therefore, a TMFS material containing CF_3 functional group and silane chain is adopted to ameliorate the perovskite/spiro-OMeTAD interface, thus contributing to a higher V_{OC} in flexible devices. The configuration of the flexible device using two interfacial modification layers (TMPU and TMFS) and the

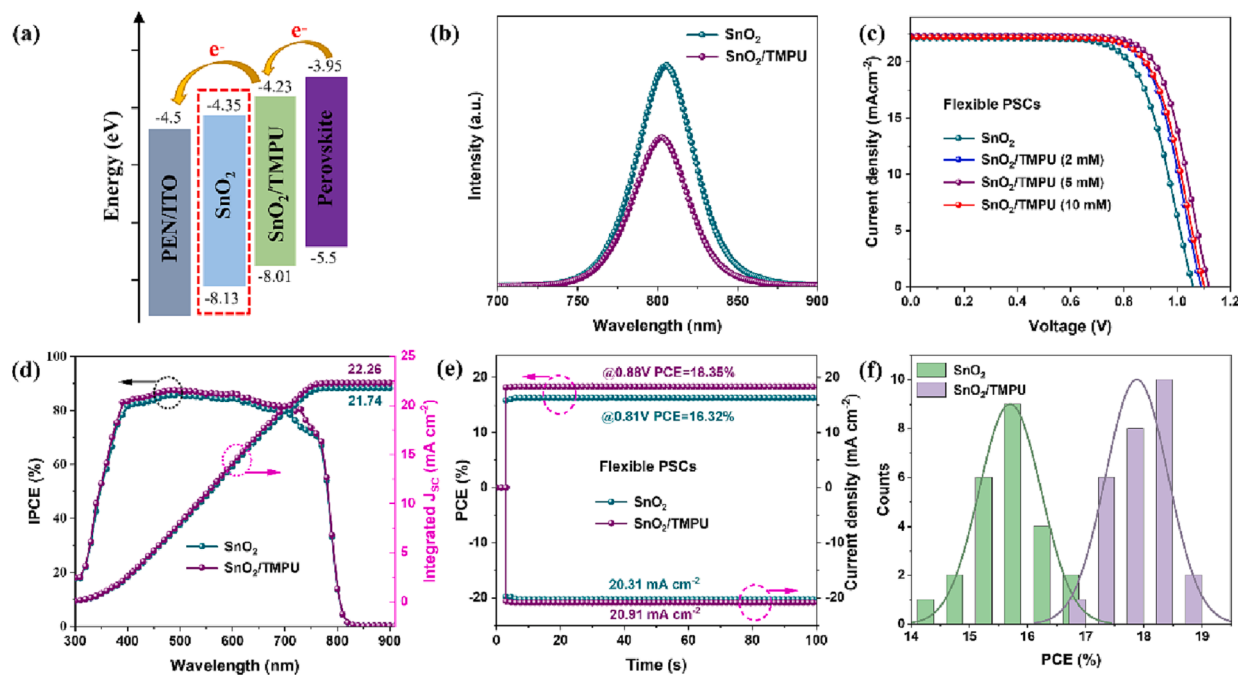


Fig. 3. (a) Energy level matching between SnO₂, SnO₂/TMPU and perovskite respectively. (b) The PL spectra of perovskite films with SnO₂ and SnO₂/TMPU. (c) J-V curves of flexible PSCs modified with various concentrations of TMPU. (d) The IPCE spectra and (e) stable power output of flexible PSCs treated with TMPU. (f) Statistical distribution of PCEs of devices based on SnO₂ and SnO₂/TMPU.

molecular structure of TMFS are depicted in Fig. 4a and b. The fluorination is reported to be an important measure to passivate surface defects and improve hydrophobicity for perovskite films ascribed to the specific effect of F atoms [41]. Compared to the single F atom, the CF₃ group with stronger electronegativity can be expected to be more effective in reducing surface defects and improving surface hydrophobicity of perovskite films [42]. The XPS and FTIR characterizations are recorded to confirm whether the TMFS is effectively deposited on the surface of the perovskite (Fig. 4c and d). The peak at 688.56 eV is determined to F element in TMFS-treated perovskite film, manifesting the existence of TMFS molecule onto the surface of perovskite film [27]. The stretching vibration peaks of Si-O and C-F bonds at 1050.09 cm⁻¹ and 1182.26 cm⁻¹ can be observed in perovskite film treated with TMFS, thus confirming that the TMFS is anchored on the surface of perovskite film [43]. The XPS is further used to reveal the chemical bond states and possible interaction between TMFS and perovskite. The XPS peak of N 1 s is shifted to higher binding energy for the perovskite film after the TMFS treatment, attributing to the formation of N-H···F hydrogen bond (Fig. 4e) [27]. The formation of strong hydrogen bond is beneficial for suppressing organic cation vacancies defects caused by volatilization of organic components under thermal annealing and stabilizing the perovskite surface [27,44]. The hole-only flexible device with the TMFS-treated perovskite absorber presents a lower N_t of 3.27 × 10¹⁵ cm⁻³ than the initial perovskite-based device (N_t = 4.36 × 10¹⁵ cm⁻³), which further proofs the lesser defect density in the TMFS-passivated perovskite film (Fig. S8) [16]. The charge transfer and recombination kinetics from perovskite layer to spiro-OMeTAD HTL are observed by the PL and TRPL spectra. As presented in Fig. 4f, the PL intensity of the TMFS-treated perovskite film is evidently lower than the control sample, indicating the more effective hole extraction and transport from perovskite to spiro-OMeTAD after TMFS modification. As exhibited in Fig. 4g, an apparent quenching process is observed in the TMFS-treated perovskite film, which is also attributed to the suppression of trap density and faster hole transfer from perovskite to spiro-OMeTAD [45]. The impacts of TMFS on the surface conditions of perovskite films are explored from KPFM measurements (Fig. 4h and i). Intriguingly, the TMFS-treated perovskite film displays lesser red high-potential areas

acting as the centers of carrier aggregation and recombination, thus further confirming the reduction of unfavorable surface defects [16]. In addition, the perovskite energy levels without and with TMFS treatment are determined from UV absorption and UPS measurements. As seen from Fig. S9, the TMFS-modified perovskite film presents the E_C and E_V positions of -3.89 eV and -5.44 eV, respectively, compared to the pristine perovskite (E_C = -3.95 eV, E_V = -5.5 eV). The energy level change of the perovskite after TMFS modification may be attributed to the dipole effect of TMFS on the surface of the perovskite film, which is beneficial to reduce energy loss at the perovskite/spiro-OMeTAD interface [45,46]. Meanwhile, the water-resistivity capability of perovskite films without and with TMFS treatment is evaluated by contact angle measurements, as depicted in Fig. S10. Encouragingly, the enhanced water contact angle is obviously observed for the perovskite film after TMFS modification, manifesting that the introduction of TMFS interface layer with hydrophobic group is beneficial for ameliorating the environmental stability of perovskite film. Particularly, the infrared thermal imaging camera (IR camera) is adopted to explore the impact of TMFS on the heat transfer of perovskite [47]. The time-evolved cooling test is performed at temperatures decreasing from 85 °C to 20 °C to evaluate the heat dissipation effect of the TMFS, where the structures of the control and target samples are PEN/ITO/perovskite/spiro-OMeTAD and PEN/ITO/perovskite/TMFS/spiro-OMeTAD, respectively (Fig. S11). The both samples are placed on a hotplate at 85 °C and then immediately moved to a 20 °C platform to observe the cooling process. Obviously, the target sample displays a lower surface temperature of 46 °C, while the control sample is about 55 °C. The faster cooling rate in the target sample elucidates that silane coupling agents may be beneficial to promote heat dissipation and ameliorate the thermal stability of flexible PSCs.

The energy band alignment diagram of different layers in the flexible PSCs with dual-interface modification layers is depicted in Fig. 5a. Apparently, The TMPU deposited on the surface of SnO₂ is beneficial to optimize the energy level alignment between SnO₂ and perovskite, while the perovskite film modified with TMFS is conducive to reducing the hole transfer barrier due to dipole effect. The underlying mechanism diagram of dual-interface engineering using TMPU and TMFS layers in

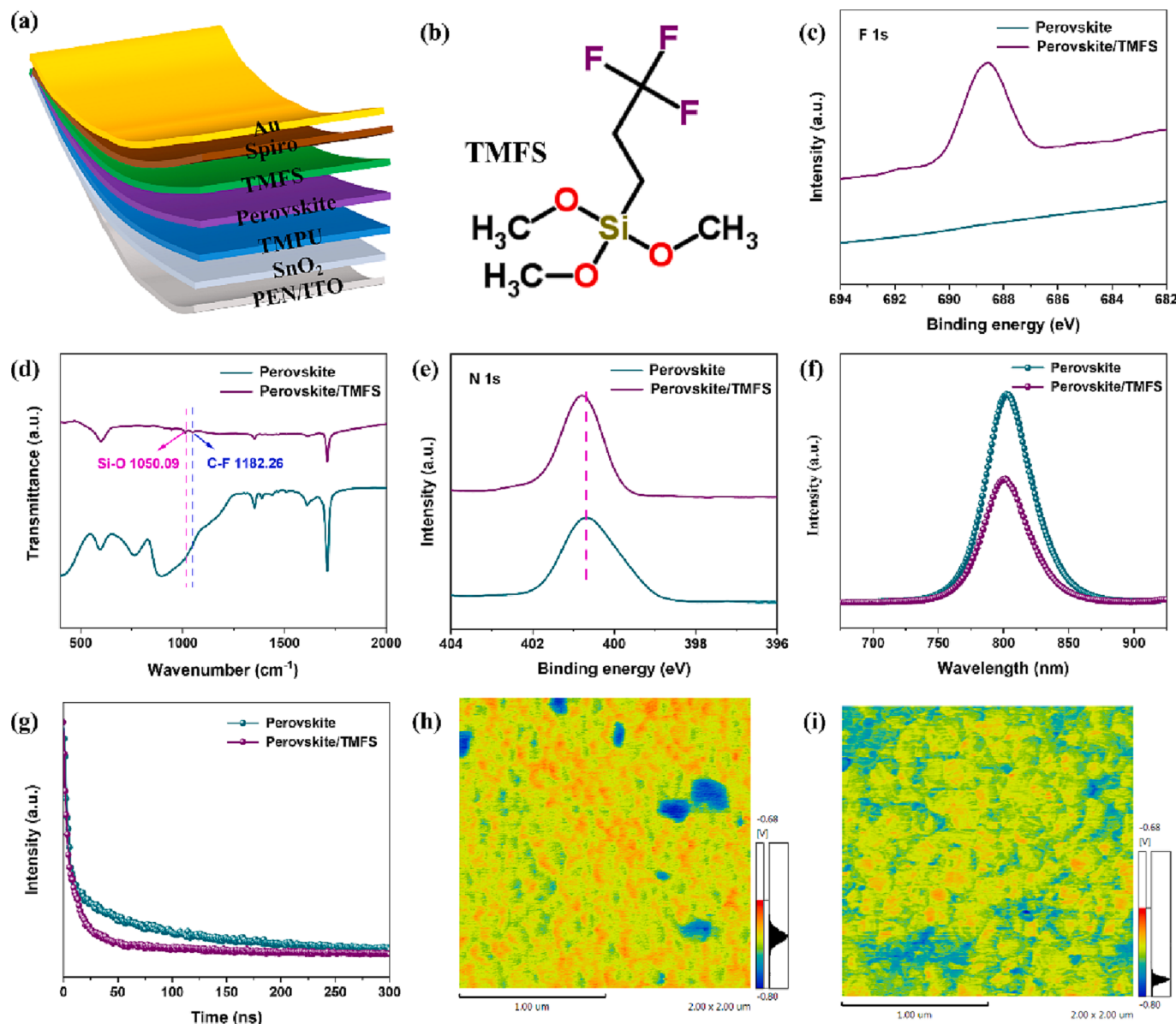


Fig. 4. (a) The structure of flexible device using dual-interface modification layers. (b) The molecular structure of TMFS material. The (c) XPS and (d) FTIR spectra of perovskite films before and after TMFS treatment. (e) The XPS spectra of N 1 s in perovskite films before and after TMFS treatment. The (f) PL and (g) TRPL of pristine and TMFS-treated perovskite films with the existence of spiro-OMeTAD. The KPFM images of (h) pristine perovskite film and (i) perovskite film modified with TMFS.

flexible PSCs is presented in Fig. 5b. The TMPU and TMFS materials are introduced to simultaneously ameliorate the SnO₂/perovskite and perovskite/spiro-OMeTAD interfaces through special effects of the multi-functional groups, thereby establishing better energy level matching as well as significantly passivating unfavorable interfacial defects and enabling faster carriers (electron and hole) extraction in flexible device. The corresponding flexible PSCs treated with different concentrations of TMFS are prepared to further evaluate the effectiveness on the PV performance enhancement based on the previously modified flexible device, as illustrated in Fig. 5c. Excitedly, the champion PCE of flexible PSCs modified with the concentration (10 mM) of TMFS is further augmented to 20.06% corresponding to a V_{OC} of 1.16 V, a J_{SC} of 22.38 mA cm^{-2} and a FF of 77.27%, which significantly outperforms than the pristine device (16.44%) without interface modification layer (Table S4). For brevity, the corresponding device employing the dual-interface engineering is labeled as target device, while the pristine device without passivation layer is unified as control device. The steady-state output measurements of these devices at maximum power

point are exhibited in Fig. 5d [48]. The stabilized PCE of 20.01% is measured for the target device, well consistent with the value measured by the J-V curves. Moreover, the integrated current value of the target device calculated by the IPCE spectra is 22.31 mA cm^{-2} , which is well accordance with the J_{SC} value extracted from the J-V characterization (Fig. 5e) [27]. The repeatability of the PV performance improvement of the target device is further verified by counting the test parameters for each group of 30 devices (Fig. S12). The hysteresis index (HI) is calculated by the J-V curve characterizations at reverse scan (RS) and forward scan (FS) conditions [49]. As displayed in Fig. 5f and Table S5, a lower HI value (0.013) is obtained in the target device compared to the control device (0.11). The corresponding rigid PSCs based on glass substrates are also prepared to assess the versatility of the above dual-interface engineering (Fig. S13). Noteworthy, the champion rigid target device with TMPU and TMFS interface layers produces an outstanding PCE of 23.11%, together with a V_{OC} of 1.18 V, a J_{SC} of 24.16 mA cm^{-2} , a FF of 81.09% and a HI of 0.87%, which is significantly superior to the unmodified control device (19.39%). The detailed PV parameters for these

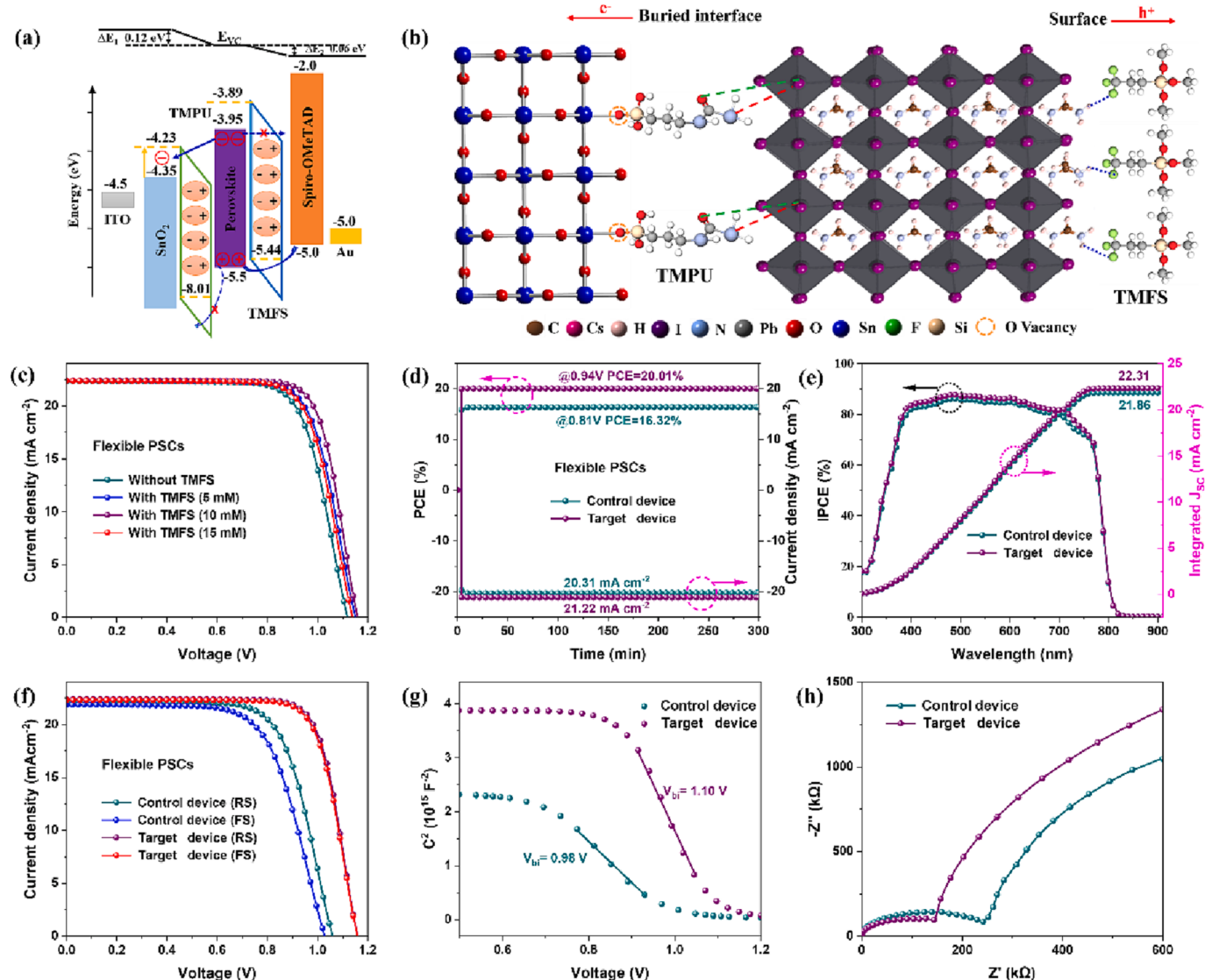


Fig. 5. (a) The schematic diagram of the flexible PSCs with TMPU and TMFS layers. (b) The functional mechanism of the dual-interface engineering using silane coupling agents (TMPU and TMFS). (c) The J-V curves of flexible devices based on SnO₂/TMPU with different concentrations of TMFS modification. (d) The stable power output and (e) IPCE spectra characterizations of the flexible devices. (f) J-V response of the flexible devices measured with FS and RS conditions. (g) The M – S plots and (h) EIS spectra measurements for the control and target devices.

rigid devices are summarized in Table S6.

To further reveal the reliability of dual-interface engineering on the performance enhancement of flexible PSCs in terms of device characterizations, the Mott–Schottky (M–S) characterizations of the control and target devices are described in Fig. 5g. Evidently, the target flexible device presents a larger built-in potential (V_{bi}) of 1.10 V, contributing to an enhanced V_{OC} for the target device [16]. Subsequently, the exponential factor (α) can be determined by performing a linear fitting to both J_{SC} and light intensity (I), as illustrated in Fig. S14 [50]. A higher α of 0.981 is observed in the target device than the control device (0.968), verifying the effective inhibition of bimolecular recombination in the target device after dual-interface modification. Besides, the correlation of obtained V_{OC} with I is investigated to determine the ideality factor (n) in flexible devices, as displayed in Fig. S15 [51]. A smaller n value of 1.38 is presented in the target device than the control device (1.71), confirming that the trap-assisted carrier recombination is significantly suppressed for the target device treated with the dual-interface engineering. Moreover, the carriers transfer and recombination kinetics in the flexible devices are explored by the electrochemical impedance spectroscopy (EIS) characterizations, as revealed in Fig. 5h. As reported,

the left semicircle and the right semicircle for flexible devices symbolize the charge transfer and recombination processes, respectively, where the size of the semicircle is proportional to the resistance of each process [16]. Obviously, the target device presents improved charge transport and suppressed charge recombination, attributing that the excellent energy level matching and remarkable defects passivation in the target device by the dual-interface modification engineering. Additionally, the dark J-V properties of the control and target devices are displayed in Fig. S16. A lower leakage current density is presented in the target device, indicating the decreased non-radiative recombination losses and conformity with the EIS conclusions [52].

The stability issues are a worrying event for the practical operation of flexible PSCs; therefore, the stability of the target device after dual-interface modification is evaluated through PCE changes in four aspects (humidity, light, temperature and bending) [53]. As exhibited in Fig. 6a, the target device without encapsulation can maintain 86.1% of the initial efficiency after storing for 3000 h at room temperature with 50 ± 5% RH, while the PCE of control device fads to 17.3% of its original value. The significantly enhanced environmental stability in the target device may be resulting from improved hydrophobicity on the surface of

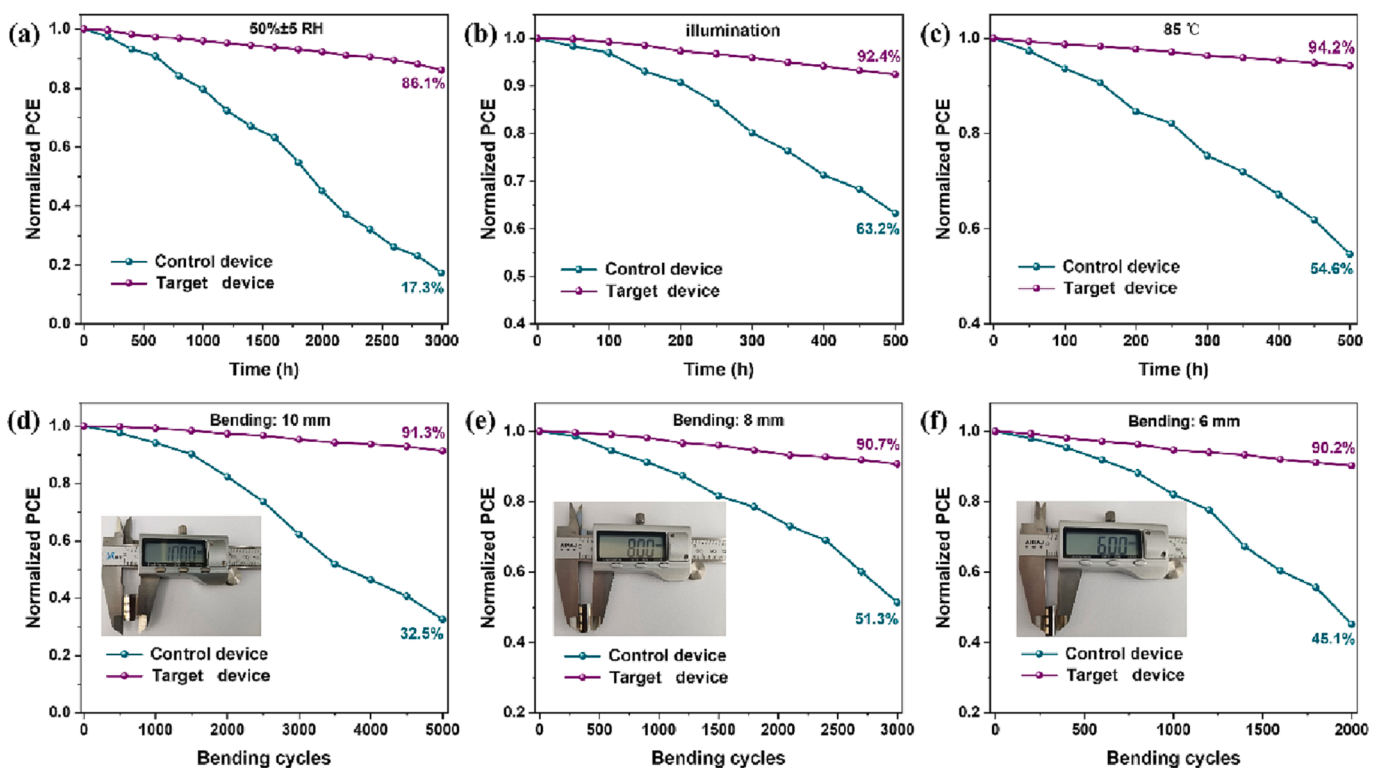


Fig. 6. (a) The environmental stability measurement of devices at 25°C, 50 ± 5% RH in the dark, (b) the illumination (AM 1.5G, 100 mW cm⁻²) and (c) temperature stability measurements at 85°C of the control and target devices without encapsulation. The bending stability characterizations of the control and target devices (unencapsulated) with bending curvature radius of (d) 10 mm, (e) 8 mm and (f) 6 mm.

the perovskite film and the reduction in unfavorable interfacial defects [54]. It is revealed that the target device can retain 92.4% of the original efficiency under continuous illumination at 100 mW cm⁻² for 500 h compared to the control device (Fig. 6b). As presented in Fig. 6c, the target device still reserves 94.2% of its original PCE after continuous heating for 500 h compared with 54.6% for the control device. The improved thermal stability for the target device may be originated from the special heat dissipation effects of silane coupling agents [47]. Moreover, the Bending stability is a unique characteristic of flexible PSCs compared to rigid devices [55]. The target device presents unprecedented bending durability, where 91.3% of its original PCE is retained after 5000 cycles with bending curvature radius of 10 mm, compared with 32.5% for the control device (Fig. 6d). Moreover, the target device still retains 90.7% of the original PCE after 3000 cycles with bending curvature radius of 8 mm, whereas the efficiency of control device decays to 51.3% (Fig. 6e). The PCE of target device can still preserve 90.2% of the original value after 2000 cycles with bending curvature radius of 6 mm, suggesting favorable interface contact and bending stability in the target device (Fig. 6f). The introduction of silane coupling agents at the two interfaces is beneficial to enhance the interfacial contact of the f-PSCs, thus improving the interfacial toughness of the f-PSCs. The above results confirm that the dual-interface engineering has positive effects on enhancing the stability of all aspects of flexible devices.

4. Conclusions

In summary, a comprehensive dual-interface engineering using two interface modification layers (TMPU and TMFS) is proposed to simultaneously ameliorate the SnO₂/perovskite and perovskite/spiro-OMeTAD interfaces toward high-performance flexible PSCs. It is demonstrated that the incorporation of TMPU on the surface of SnO₂ is conducive to reducing the detrimental defects of SnO₂ by forming Sn-O-Si bonds and passivate the bottom defects of perovskite, thus enhancing

the electrical properties of SnO₂ and obtaining improved perovskite film quality. Meanwhile, the hydrophobic material TMFS deposited onto the surface of perovskite film is conducive to suppressing detrimental interfacial defects by forming hydrogen bonds and increasing the environmental stability of perovskite film. Benefiting from these positive effects, the target device treated with the dual-interface engineering presents excellent energy-level matching and promoted charge transfer, thereby significantly reducing the non-radiative combination loss in the target device. Consequently, the corresponding flexible and rigid target device achieve outstanding PCE of 20.06% and 23.11%, respectively, which outperform that of control devices. More importantly, the use of dual-interface engineering is pivotal to improving the stability of the device, especially the bending durability. The successful dual-interface engineering in this study provides a promising direction for achieving high-performance flexible PSCs toward commercial application.

Declaration of Competing Interest

The authors declare that they have no known competing financial interests or personal relationships that could have appeared to influence the work reported in this paper.

Data availability

The authors do not have permission to share data.

Acknowledgments

This research was financially supported by the National Key Research and Development Program of China (nos. 2020YFA0715000). The authors thank the Analytical and Testing Center of Huazhong University Science and Technology for the technical assistance. The authors also thank the technical assistance of the Nanoscale Characterization & Devices (CNCD) Center of Wuhan National Laboratory for

Optoelectronics. The sample measurements from the Souspad company are likewise gratefully acknowledged. The research facilities of Suzhou Fangsheng FS-300 are equally appreciated.

Appendix A. Supplementary data

Supplementary data to this article can be found online at <https://doi.org/10.1016/j.cej.2023.143790>.

References

- [1] H.S. Jung, G.S. Han, N.-G. Park, M.J. Ko, Flexible perovskite solar cells, Joule 3 (8) (2019) 1850–1880.
- [2] K. Li, X. Yang, F. Yang, J. He, G. Zhang, S. Jiang, C. Chen, J. Tang, Flexible short-wavelength infrared photodetector based on extrinsic Sb_2Se_3 , Mater. Today Electron. 2 (2022) 100011.
- [3] L. Yang, J. Feng, Z. Liu, Y. Duan, S. Zhan, S. Yang, K. He, Y. Li, Y. Zhou, N. Yuan, J. Ding, S. Liu, Record-efficiency flexible perovskite solar cells enabled by multifunctional organic ions interface passivation, Adv. Mater. 34 (2022) 2201681.
- [4] L. Yang, H. Zhou, Y. Duan, M. Wu, K. He, Y. Li, D. Xu, H. Zou, S. Yang, Z. Fang, S. Liu, Z. Liu, 25.24%-Efficiency FACsPbI_3 perovskite solar cells enabled by intermolecular esterification reaction of DL-carnitine hydrochloride, Adv. Mater. 35 (2023) 2211545.
- [5] Y. Chen, Z. Gao, F. Zhang, Z. Wen, X. Sun, Recent progress in self-powered multifunctional e-skin for advanced applications, Exploration 2 (2022) 20210112.
- [6] J. Zhang, W. Zhang, H.M. Cheng, S.R.P. Silva, Critical review of recent progress of flexible perovskite solar cells, Mater. Today 39 (2020) 66–88.
- [7] M. Li, J. Zhou, L. Tan, H. Li, Y. Liu, C. Jiang, Y. Ye, L. Ding, W. Tress, C. Yi, Multifunctional succinate additive for flexible perovskite solar cells with more than 23% power-conversion efficiency, Innovation 3 (2022) 100310.
- [8] H. Min, D.Y. Lee, J. Kim, G. Kim, K.S. Lee, J. Kim, M.J. Paik, Y.K. Kim, K.S. Kim, M. G. Kim, T.J. Shin, S. Il Seok, Perovskite solar cells with atomically coherent interlayers on SnO_2 electrodes, Nature 598 (2021) 444–450.
- [9] S. Zhang, X. Yan, Z. Liu, H. Zhu, Z. Yang, Y. Huang, S. Liu, D. Wu, M. Pan, W. Chen, Evaporated potassium chloride for double-sided interfacial passivation in inverted planar perovskite solar cells, J. Energy Chem. 54 (2021) 493–500.
- [10] B. Zong, D. Hu, Q. Sun, J. Deng, Z. Zhang, X. Meng, B. Shen, B. Kang, S.R.P. Silva, G. Lu, 2, 3, 4, 5, 6-Pentafluorophenylammonium bromide-based double-sided interface engineering for efficient planar heterojunction perovskite solar cells, Chem. Eng. J. 452 (2023) 139308.
- [11] X. Chen, W. Xu, Z. Shi, G. Pan, J. Zhu, J. Hu, X. Li, C. Shan, H. Song, Europium ions doped WO_x nanorods for dual interfacial modification facilitating high efficiency and stability of perovskite solar cells, Nano Energy 80 (2021) 105564.
- [12] F. Zhang, S. Ye, H. Zhang, F. Zhou, Y. Hao, H. Cai, J. Song, J. Qu, Comprehensive passivation strategy for achieving inverted perovskite solar cells with efficiency exceeding 23% by trap passivation and ion constraint, Nano Energy 89 (2021) 106370.
- [13] S. You, H. Zeng, Z. Ku, X. Wang, Z. Wang, Y. Rong, Y. Zhao, X. Zheng, L. Luo, L. Li, S. Zhang, M. Li, X. Gao, X. Li, Multifunctional polymer-regulated SnO_2 nanocrystals enhance interface contact for efficient and stable planar perovskite solar cells, Adv. Mater. 32 (2020) 2003990.
- [14] W. Ke, G. Fang, Q. Liu, L. Xiong, P. Qin, H. Tao, J. Wang, H. Lei, B. Li, J. Wan, G. Yang, Y. Yan, Lowerature solution-processed tin oxide as an alternative electron transporting layer for efficient perovskite solar cells, J. Am. Chem. Soc. 137 (2015) 6730–6733.
- [15] P. Zeng, W. Deng, M. Liu, Recent advances of device components toward efficient flexible perovskite solar cells, Sol. RRL 4 (2020) 1900485.
- [16] Z. Yi, X. Li, B. Xiao, Y. Luo, Q. Jiang, J. Yang, Large improvement of photovoltaic performance of flexible perovskite solar cells using a multifunctional phosphoethanolamine-modified SnO_2 layer, Sci. China Mater. 65 (2022) 3392–3401.
- [17] Y. Zhang, L. Xu, Y. Wu, Q. Zhou, Z. Shi, X. Zhuang, B. Liu, B. Dong, X. Bai, W. Xu, D. Zhou, H. Song, Double-layer synergistic optimization by functional black phosphorus quantum dots for high-efficiency and stable planar perovskite solar cells, Nano Energy 90 (2021) 106610.
- [18] F. Hao, Dimensional tailoring endows tin halide perovskite solar cells with high efficiency and stability, Mater. Lab. 1 (2022) 20220047.
- [19] X. Yang, D. Luo, Y. Xiang, L. Zhao, M. Anaya, Y. Shen, J. Wu, W. Yang, Y.H. Chiang, Y. Tu, R. Su, Q. Hu, H. Yu, G. Shaw, W. Huang, T.P. Russell, Q. Gong, S.D. Stranks, W. Zhang, R. Buried interfaces in halide perovskite photovoltaics, Adv. Mater. 33 (2021) 2006435.
- [20] J. Wu, Z. Ma, S. Huang, Y. Lei, H. Guo, Y. Fang, D. Xie, N. Fu, Y. Lin, Directly purifiable Pre-oxidation of Spiro-OMeTAD for stability enhanced perovskite solar cells with efficiency over 23%, Chem. Eng. J. 437 (2022) 135457.
- [21] N. Li, S. Tao, Y. Chen, X. Niu, C.K. Onwudinanti, C. Hu, Z. Qiu, Z. Xu, G. Zheng, L. Wang, Y. Zhang, L. Li, H. Liu, Y. Lun, J. Hong, X. Wang, Y. Liu, H. Xie, Y. Gao, Y. Bai, S. Yang, G. Brocks, Q. Chen, H. Zhou, Cation and anion immobilization through chemical bonding enhancement with fluorides for stable halide perovskite solar cells, Nat. Energy 4 (2019) 408–415.
- [22] J. Zheng, F. Li, C. Chen, Q. Du, M. Jin, H. Li, M. Ji, Z. Shen, Perovskite solar cells employing a $\text{PbSO}_4(\text{PbO})_4$ quantum dot-doped spiro-OMeTAD hole transport layer with an efficiency over 22%, ACS Appl. Mater. Interfaces 14 (2) (2022) 2989–2999.
- [23] Y. Zhang, L. Xu, J. Sun, Y. Wu, Z. Kan, H. Zhang, L. Yang, B. Liu, B. Dong, X. Bai, H. Song, 24.11% high performance perovskite solar cells by dual interfacial carrier mobility enhancement and charge-carrier transport balance, Adv. Energy Mater. 12 (2022) 2201269.
- [24] X. Zhang, C. Cao, Y. Bai, C. Zhu, H. Zai, S. Ma, Y. Chen, Z. Cui, C. Shi, C. Wang, C. Zhou, G. Yuan, Z. Gao, J. Hong, J. Dou, H. Wang, H. Zhou, H. Xiao, J. Li, Q. i. Chen, Impeded degradation of perovskite solar cells via the dual interfacial modification of siloxane, Sci. China Chem. 65 (11) (2022) 2299–2306.
- [25] C.C. Zhang, S. Yuan, Y.H. Lou, Q.W. Liu, M. Li, H. Okada, Z.K. Wang, Perovskite films with reduced interfacial strains via a molecular-level flexible interlayer for photovoltaic application, Adv. Mater. 32 (2020) 2001479.
- [26] F. Ali, C. Roldán-Carmona, M. Sohail, M.K. Nazeeruddin, Applications of self-assembled monolayers for perovskite solar cells interface engineering to address efficiency and stability, Adv. Energy Mater. 10 (2020) 2002989.
- [27] Z. Yi, B. Xiao, X. Li, Y. Luo, Q. Jiang, J. Yang, Revealing the interfacial properties of halide ions for efficient and stable flexible perovskite solar cells, J. Colloid Interface Sci. 628 (2022) 696–704.
- [28] Y. Tan, B.o. Xiao, P. Xu, Y. Luo, Q. Jiang, J. Yang, Improving the photovoltaic performance of flexible solar cells with semitransparent inorganic perovskite active layers by interface engineering, ACS Appl. Mater. Interfaces 13 (17) (2021) 20034–20042.
- [29] L. Liu, Y. Li, C. Zheng, Z. Liu, N. Yuan, J. Ding, D. Wang, S. Liu, Collaborative strategy of multifunctional groups in trifluoroacetamide achieving efficient and stable perovskite solar cells, Sol. RRL 6 (2022) 2200284.
- [30] Y. Shi, H. Zhang, X. Tong, X. Hou, F. Li, Y. Du, S. Wang, Q. Zhang, P. Liu, X. Zhao, Interfacial engineering via self-assembled thiol silane for high efficiency and stability perovskite solar cells, Sol. RRL 5 (2021) 2100128.
- [31] Z. Dai, S.K. Yadavalli, M. Chen, A. Abbaspourtanjani, Y. Qi, N.P. Padture, Interfacial toughening with self-assembled monolayers enhances perovskite solar cell reliability, Science 372 (6542) (2021) 618–622.
- [32] Y. Duan, K. He, L. Yang, J. Xu, W. Zhao, Z. Liu, 24.20%-efficiency MA-free perovskite solar cells enabled by siloxane derivative interface engineering, Small 18 (2022) 2204733.
- [33] Y. Che, Z. Liu, Y. Duan, J. Wang, S. Yang, D. Xu, W. Xiang, T. Wang, N. Yuan, J. Ding, S. Liu, Hydrazide derivatives for defect passivation in pure CsPbI_3 perovskite solar cells, Angew. Chem. Int. Ed. 61 (2022) e202205012.
- [34] M. Zhong, Y. Liang, J. Zhang, Z. Wei, Q.i. Li, D. Xu, Highly efficient flexible MAPbI_3 solar cells with a fullerene derivative-modified SnO_2 layer as the electron transport layer, J. Mater. Chem. A 7 (12) (2019) 6659–6664.
- [35] T. Bu, J. Li, F. Zheng, W. Chen, X. Wen, Z. Ku, Y. Peng, J. Zhong, Y.B. Cheng, F. Huang, Universal passivation strategy to slot-die printed SnO_2 for hysteresis-free efficient flexible perovskite solar module, Nat. Commun. 9 (2018) 4609.
- [36] Y.R. Shi, K.L. Wang, Y.H. Lou, D.B. Zhang, C.H. Chen, J. Chen, Y.X. Ni, S. Öz, Z. K. Wang, L.S. Liao, Unraveling the role of active hydrogen caused by carbonyl groups in surface-defect passivation of perovskite photovoltaics, Nano Energy 97 (2022) 107200.
- [37] G. Liu, H. Zheng, L. Zhang, H. Xu, S. Xu, X. Xu, Z. Liang, X. Pan, Tailoring multifunctional passivation molecules with halogen functional groups for efficient and stable perovskite photovoltaics, Chem. Eng. J. 407 (2021) 127204.
- [38] T. Li, S. Wang, J. Yang, X. Pu, B. Gao, Z. He, Q. Cao, J. Han, X. Li, Multiple functional groups synergistically improve the performance of inverted planar perovskite solar cells, Nano Energy 82 (2021) 105742.
- [39] R. Zhao, L. Xie, R. Zhuang, T. Wu, R. Zhao, L. Wang, L. Sun, Y. Hua, Interfacial defect passivation and charge carrier management for efficient perovskite solar cells via a highly crystalline small molecule, ACS Energy Lett. 6 (12) (2021) 4209–4219.
- [40] P. Zhu, S. Gu, X. Luo, Y. Gao, S. Li, J. Zhu, H. Tan, Simultaneous contact and grain-boundary passivation in planar perovskite solar cells using $\text{SnO}_2\text{-KCl}$ composite electron transport layer, Adv. Energy Mater. 10 (2020) 1903083.
- [41] H. Wang, J. Du, X. Li, H. Duan, S. Yang, D. Han, J. Yang, L. Fan, F. Wang, L. Yang, Reinforcing perovskite framework via aminotri fluorotoluene for achieving efficient and moisture-resistance solar cells, Chem. Eng. J. 450 (2022) 137990.
- [42] B. Li, Y. Cai, X. Tian, X. Liang, D. Li, Z. Zhang, S. Wang, K. Guo, Z. Liu, Decorating hole transport material with $-\text{CF}_3$ groups for highly efficient and stable perovskite solar cells, J. Energy Chem. 62 (2021) 523–531.
- [43] Y. Bai, Q. Dong, Y. Shao, Y. Deng, Q. Wang, L. Shen, D. Wang, W. Wei, J. Huang, Enhancing stability and efficiency of perovskite solar cells with crosslinkable silane-functionalized and doped fullerenes, Nat. Commun. 7 (2016) 12806.
- [44] X. Gong, H. Li, R. Zhou, X. Peng, Y. Ouyang, H. Luo, X. Liu, J. Zhuang, H. Wang, Y. Ni, Y. Lei, Strong electron acceptor of a fluorine-containing group leads to high performance of perovskite solar cells, ACS Appl. Mater. Interfaces 13 (34) (2021) 41149–41158.
- [45] B. Wang, H. Li, Q. Dai, M. Zhang, Z. Zou, J.L. Brédas, Z. Lin, Robust molecular dipole-enabled defect passivation and control of energy-level alignment for high-efficiency perovskite solar cells, Angew. Chem. Int. Ed. 60 (2021) 7664–17670.
- [46] H. Liu, Z. Lu, W. Zhang, J. Wang, Z. Lu, Q. Dai, X. Qi, Y. Shi, Y. Hua, R. Chen, T. Shi, H. Xia, H.L. Wang, Anchoring vertical dipole to enable efficient charge extraction for high-performance perovskite solar cells, Adv. Sci. 9 (2022) 2203640.
- [47] F. Pei, N. Li, Y. Chen, X. Niu, Y.u. Zhang, Z. Guo, Z. Huang, H. Zai, G. Liu, Y. Zhang, Y. Bai, X. Zhang, C. Zhu, Q.i. Chen, Y. Li, H. Zhou, Thermal management enables more efficient and stable perovskite solar cells, ACS Energy Lett. 6 (9) (2021) 3029–3036.
- [48] Y. Zhong, C. Li, G. Xu, C. Xu, J. Dong, D. Liu, D. Lu, J. You, C. Gao, Q. Song, Collaborative strengthening by multi-functional molecule 3-thiophenboronic acid for efficient and stable planar perovskite solar cells, Chem. Eng. J. 436 (2022) 135134.

- [49] X. Li, Y. Meng, R. Liu, Z. Yang, Y. Zeng, Y. Yi, W.E.I. Sha, Y. Long, J. Yang, High-efficiency and durable inverted perovskite solar cells with thermally-induced phase-change electron extraction layer, *Adv. Energy Mater.* 11 (2021) 2102844.
- [50] Z. Shi, D. Zhou, Y. Wu, G. Pan, W. Xu, N. Wang, S. Liu, R. Sun, L. Liu, X. Zhuang, Y. Zhang, S. Lu, H. Song, Dual interfacial engineering to improve ultraviolet and near-infrared light harvesting for efficient and stable perovskite solar cells, *Chem. Eng. J.* 435 (2022) 134792.
- [51] Z. Yi, T. Zhang, H. Ban, H. Shao, X. Gong, M. Wu, G. Liang, X.L. Zhang, Y. Shen, M. Wang, AgBi₃I₁₀ ruddriffite for photovoltaic application, *Sol. Energy* 206 (2020) 436–442.
- [52] X. Wang, W. Sun, Y. Tu, Q. Xiong, G. Li, Z. Song, Y. Wang, Y. Du, Q. Chen, C. Deng, Z. Lan, P. Gao, J. Wu, Lansoprazole, a cure-four, enables perovskite solar cells efficiency exceeding 24%, *Chem. Eng. J.* 446 (2022) 137416.
- [53] Z. Dai, S. Li, X. Liu, M. Chen, C.E. Athanasiou, B.W. Sheldon, H. Gao, P. Guo, N. P. Padture, Dual-interface-reinforced flexible perovskite solar cells for enhanced performance and mechanical reliability, *Adv. Mater.* 34 (2022) 2205301.
- [54] H.B. Lee, N. Kumar, V. Devaraj, B. Tyagi, S. He, R. Sahani, K.J. Ko, J.W. Oh, J. W. Kang, Trifluoromethyl-group bearing, hydrophobic bulky cations as defect passivators for highly efficient, stable perovskite solar cells, *Sol. RRL* 5 (2021) 2100712.
- [55] J. Wu, P. Chen, H. Xu, M. Yu, L. Li, H. Yan, Y. Huangfu, Y. Xiao, X. Yang, L. Zhao, W. Wang, Q. Gong, R. Zhu, Ultralight flexible perovskite solar cells, *Sci. China Mater.* 65 (2022) 2319–2324.